

**Extensibility governs the flow-induced alignment of polymers and rod-like colloids**Vincenzo Calabrese<sup>1,\*</sup>, Tatiana Porto Santos<sup>1</sup>, Carlos G. Lopez<sup>2</sup>, Minne Paul Lettinga<sup>3,4</sup>,  
Simon J. Haward<sup>1</sup> and Amy Q. Shen<sup>1</sup><sup>1</sup>*Micro/Bio/Nanofluidics Unit, Okinawa Institute of Science and Technology Graduate University, 1919-1 Tancha, Onna-son, Okinawa 904-0495, Japan*<sup>2</sup>*RWTH Aachen University, Institute of Physical Chemistry, Landoltweg 2, 52074 Aachen, Germany*<sup>3</sup>*Laboratory for Soft Matter and Biophysics, KU Leuven, Celestijnenlaan 200D, B-3001 Leuven, Belgium*<sup>4</sup>*ICS-3, Institut für Weiche Materie, Forschungszentrum Jülich, D-52425 Jülich, Germany*

(Received 23 July 2023; accepted 29 January 2024; published 26 February 2024)

Polymers and rod-like colloids (PaRC) adopt a favorable orientation under sufficiently strong flows. However, how the flow kinematics affect the alignment of such nanostructures according to their extensibility remains unclear. By analyzing the shear- and extension-induced alignment of chemically and structurally different PaRC, we show that extensibility is a key determinant of the structural response to the imposed kinematics. We propose a unified description of the effectiveness of extensional flow, compared to shearing flow, at aligning PaRC of different extensibility.

DOI: [10.1103/PhysRevResearch.6.L012042](https://doi.org/10.1103/PhysRevResearch.6.L012042)

Polymers and rod-like colloids (PaRC) are ubiquitous in biological fluids (e.g., mucus, saliva), food and industrial formulations (e.g., gels, paints), imparting specific properties and functionalities. When solubilized or dispersed in a solvent, PaRC adopt an equilibrium conformation (e.g., rod-like, worm-like, coil-like) that depends on a multitude of factors including surface chemistry, contour length, and backbone rigidity, affecting the PaRC extensibility and flexibility [1]. The PaRC extensibility  $L_e$  describes the ratio between the contour length of the fully extended structure  $l_c$  and the respective size at equilibrium. The PaRC flexibility  $N_p$  represents the number of persistence length  $l_p$  segments composing the PaRC contour length [1,2]. For rigid colloidal rods  $L_e \rightarrow 1$  and  $N_p \ll 1$ , whilst for flexible polymers that adopt a coil-like conformation at equilibrium,  $L_e \gg 1$  and  $N_p \gg 1$ . Under sufficiently strong imposed flows, PaRC are driven out of equilibrium and towards a state of alignment induced by velocity gradients in the flow field. Flow-induced alignment of PaRC is central to processes including fiber spinning [3], bacteriophage replication [4,5], and amyloid fibrillogenesis [6,7]. The link between the PaRC conformation and the bulk fluid properties at equilibrium, such as the zero-shear viscosity and the macromolecular time scales of diffusion and relaxation, are well understood and described by generalized scaling theories [1,2,8]. Nonetheless, how the dynamics of PaRC under flow depend on their equilibrium conformation

remains elusive. It is known that rigid colloidal rods tend to adopt a favorable orientation under characteristic deformation rates  $|E|$  able to overcome the rotational Brownian diffusion [2,9–11]. This condition is captured by the rotational Péclet number  $Pe = |E|/D_r \gtrsim 1$ , with  $D_r$  the rotational diffusion coefficient of the rods [2,12]. For sufficiently strong shear flows ( $Pe \gtrsim 1$ ), rigid colloidal rods orient but also undergo occasional tumbling due to the vorticity component of the strain rate tensor [13,14]. On the contrary, pure extensional flows are vorticity-free and generally regarded as more effective than shear flows at inducing the alignment of rigid colloidal rods [10,15–18]. For flexible polymers in solution, favorable chain orientation is expected to occur at Weissenberg number  $Wi = |E|\tau \gtrsim 0.5$ , with  $\tau$  the longest relaxation time of the polymer [19–22]. Extensional flows are considered pivotal at inducing a preferential orientation of flexible polymers. Direct single-molecule imaging of  $\lambda$ -DNA ( $L_e \sim 13$ ) has shown that extensional flows provide a greater extent of chain extension than shear flows [23,24]. For solutions of even more highly flexible synthetic polymers [e.g., poly(ethylene oxide) and atactic-polystyrene with  $L_e > 50$ ], microfluidic studies reporting flow-induced birefringence (FIB) show that macromolecular alignment is dominant in localized regions originating from hyperbolic points in the flow field where purely extensional kinematics are approximated [20,25–27]. From the existing literature it can be qualitatively inferred that extensional flows provide a greater level of PaRC alignment than shear flows, however a generalized and quantitative comparison has yet to be established.

In this Letter we tackle this problem by investigating the steady shear- and extension-induced alignment of PaRC with varying extensibility, including rod-like colloids and significantly more flexible polyelectrolytes in solution. Employing quantitative FIB imaging in a specific microfluidic device, we show that different deformation rates are required for the

\*Corresponding author: [vincenzo.calabrese@oist.jp](mailto:vincenzo.calabrese@oist.jp)

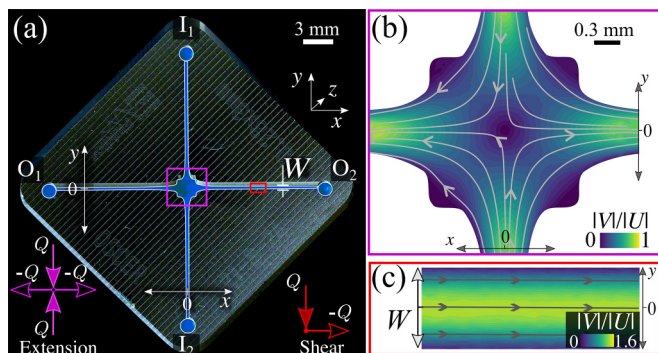


FIG. 1. (a) A photograph of the OSCER device with the extension- and shear-dominated ROI marked by the magenta and red box, respectively. Flow fields for a Newtonian fluid at  $Re < 1$  in the extension- and shear-dominated ROI in (b) and (c), respectively. The measured velocity magnitude  $|V|$  is scaled by the average flow velocity  $|U|$ .

onset of PaRC alignment in shear and extension, and that the difference is correlated with the PaRC extensibility. In the limit of rigid rod-like nanostructures we validate our results with the revised Doi-Edwards theory proposed by Lang *et al.* [11] that accounts for the flow-induced dilation of the confinement. Our study aims toward unifying the relationship between shear- and extension-induced alignment of PaRC with various extensibility.

PaRC alignment is evaluated via FIB imaging performed on a CRYSTA PI-1P camera (Photron Ltd, Japan) fitted with a  $4\times$  Nikon objective lens. Microparticle image velocimetry (PIV) (TSI Inc., MN,  $4\times$  and  $10\times$  Nikon Objectives) is used to characterize the nature of the imposed flow kinematics in the microfluidic device [28]. The microfluidic device [Fig. 1(a)], fabricated in fused silica glass [29], is a numerically optimized version of the cross-slot device, referred to as the optimized shape cross-slot extensional rheometer (OSCER) [25,26]. The device has an aspect ratio  $H/W = 10$ , where  $H = 3$  mm is the height, defining the optical path along the  $z$  axis, and  $W = 0.3$  mm is the width, producing a good approximation to a two-dimensional flow. FIB and PIV are evaluated at the  $x$ - $y$  plane in two distinct regions of interest (ROI) of the microfluidic device generating extension- or shear-dominated flows [marked by the colored boxes in Fig. 1(a)]. In the extension-dominated ROI [magenta box, Fig. 1(a)], FIB and PIV are evaluated around the stagnation point (i.e.,  $x = y = 0$  mm) where a constant and shear-free planar extension is generated when opposing inlets ( $I_1, I_2$ ) and outlets ( $O_1, O_2$ ) operate at equal and opposite volumetric flow rates ( $Q$  m<sup>3</sup>/s) [representative flow field in Fig. 1(b)]. A shear-dominated ROI [red box, Fig. 1(a)] located in one of the OSCER branches is evaluated while one inlet ( $I_1$ ) and outlet ( $O_2$ ) operate at an equal and opposite flow rate, generating a shear-dominated flow without a stagnation point [representative flow field in Fig. 1(c)]. Flow is controlled by syringe pumps (Nemesys, Cetoni) to impose an average flow velocity  $|U| = Q/(HW)$  and, typically, a Reynolds number  $Re = \rho|U|W/\eta \lesssim 1$ , with  $\rho$  the fluid density and  $\eta$  the shear viscosity at a nominal shear rate  $Q/(W^2H)$  [28]. The relatively small size of the PaRC investigated [ $l_c \sim 0.1$   $\mu$ m] ensures a

Stokes flow regime around the PaRC, thus a particle Reynolds number  $Re_p = \rho|E|l_c^2/\eta_s \ll 1$ .

The PaRC investigated in this work include rod-like colloids that are cellulose nanocrystals (CNC), oxidized cellulose nanofibrils (OCNF), protein nanofibrils (PNF), and two types of filamentous viruses (Pf1 and fd) [28]. We use carboxymethyl cellulose sodium salt (CMC) and hyaluronic acid sodium salt (HA) with distinct molecular weight ( $M_w$ ), and double stranded calf-thymus DNA sodium salt (ct-DNA) with  $\sim 28$  kbp as polyelectrolytes in solution [28]. CMC with  $M_w$  of 0.4, 0.6, and 0.8 MDa are referred to as CMC04, CMC06, and CMC08, respectively, and HA with  $M_w$  of 0.9, 1.6, 2.6, and 4.8 MDa are referred to as HA09, HA16, HA26, and HA48, respectively [30]. For the rod-like colloids, the characteristic contour length  $\langle l_c \rangle$  and the persistence length  $l_p$  are obtained from atomic force microscopy (AFM) [28,31]. For CMC and HA,  $l_p$  is obtained from the literature [32–34], and  $\langle l_c \rangle = Na$ , where  $N$  is the weight-averaged degree of polymerization, and  $a$  is the monomer length [28]. For ct-DNA,  $\langle l_c \rangle$  is obtained by multiplying the number of base pairs with their average separation distance (0.34 nm) and  $l_p = 50$  nm [21,35]. The concentrations of the PaRC are chosen to be as low as possible yet sufficient to provide a detectable birefringence signal, resulting in PaRC concentrations between the dilute and semidilute regime (see Supplemental Material for estimations of the overlap concentration [28]). Where required, the relaxation time of PaRC  $\tau$  is increased by adding glycerol or sucrose to the aqueous solvent, shifting the onset of PaRC alignment within the experimental window of accessible deformation rates. The extensibility of the PaRC is computed as  $L_e = \langle l_c \rangle / \sqrt{\langle R^2 \rangle}$ , where  $\langle R^2 \rangle = 2l_p\langle l_c \rangle - 2l_p^2[1 - \exp(-\langle l_c \rangle/l_p)]$  is the mean-squared end-to-end length of PaRC at equilibrium using a worm-like chain model [1]. The critical length scale  $\ell$  below which PaRC follow a rod-like behavior (i.e.,  $\sqrt{\langle R^2 \rangle} \propto \ell$ ) denotes the persistence length  $l_p$ . The PaRC flexibility  $N_p = \langle l_c \rangle/l_p$ , is related to  $L_e$  via

$$L_e = \sqrt{\frac{N_p^2}{2(N_p + \exp(-N_p) - 1)}}, \quad (1)$$

which approaches the scaling  $L_e \propto N_p^{0.5}$  for large  $N_p$ .

FIB patterns in the extension- and shear-dominated ROI acquired at an equal average flow velocity  $|U|$  are shown in Fig. 2 for representative PaRC with distinct  $L_e$ . For each system and ROI investigated, the birefringence ( $\Delta n$ ), probing the extent of fluid anisotropy due to the PaRC alignment, is normalized by the maximum birefringence ( $\Delta n_{\max}$ ). For fd and Pf1 a diamond-like pattern of intense birefringence is shown in the extension-dominated ROI as previously shown for colloidal rods with  $L_e \sim 1$  [15,16]. For the comparatively more extensible CMC08 ( $L_e \sim 7$ ), the diamond-like birefringence pattern fades and an intense birefringent strand develops along the extensional (i.e.,  $x$ ) axis. For the most extensible PaRC investigated, HA48 ( $L_e \sim 16$ ), the diamond-like birefringence pattern disappears and only the intense birefringent strand becomes visible. Fluid elements accumulate strain exponentially as they enter the extensional ROI and approach the extension axis [26]. Thus, more extensible PaRC need to pass close to the stagnation point to accumulate enough strain to stretch,

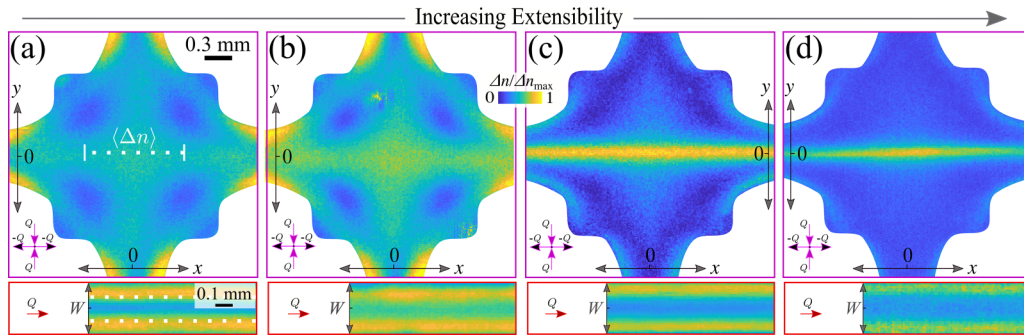


FIG. 2. Steady-state birefringence patterns for PaRC with different  $L_e$  at an equal average flow velocity ( $|U|$ ) in the extension- and shear-dominated ROI (top and bottom panels, respectively). For each system and ROI, the birefringence ( $\Delta n$ ) is normalized by the maximum birefringence ( $\Delta n_{\max}$ ). (a) fd dispersion (0.2 mg/mL,  $L_e \sim 1$ ) at  $|U| = 3.6$  mm/s. (b) Pf1 dispersion (0.1 mg/mL,  $L_e \sim 2$ ) at  $|U| = 1.9$  mm/s. (c) CMC08 solution (0.1 mg/mL,  $L_e \sim 7$ ) at  $|U| = 95.7$  mm/s. (d) HA48 solution (1 mg/mL,  $L_e \sim 16$ ) at  $|U| = 1.9$  mm/s.

leading to a localized birefringent strand. Contrarily, more rigid rod-like PaRC require a relatively small accumulated strain to align, leading to a significant alignment even away from the stagnation point, resulting in a diamond-like birefringence pattern. In the shear-dominated ROI, the birefringence increases from the centerline to the channel walls, in qualitative agreement with the trend of shear rate  $|\dot{\gamma}|$  retrieved from PIV [28]. To quantify the difference between shear- and extension-induced alignment of PaRC with distinct extensibility, we spatially average the birefringence ( $\langle \Delta n \rangle$ ) in specific locations of the shear- and extension-dominated ROI where the shear and extension deformation rates are constant. In the extension-dominated ROI, the birefringence is averaged along 1 mm of the extension axis [i.e., at  $y = 0$  for  $-0.5 < x < 0.5$ , dotted line in Fig. 2(a), top panel] and plotted as a function of the extension rate  $|\dot{\epsilon}|$  along the same line (determined from the flow field measured by PIV). In the shear-dominated ROI, the birefringence is averaged along the  $x$  direction at  $y = \pm W/4$  [marked by the dotted line in Fig. 2(a), bottom panel] and plotted as a function of the respective shear rate at the same location  $|\dot{\gamma}|$  [28]. We note that the same flow strength for shear and planar extension is given by the magnitude of the strain rate tensor as  $|\dot{\gamma}| = 2|\dot{\epsilon}|$ .

In Fig. 3 we plot the normalized birefringence,  $\langle \Delta n \rangle / \phi$ , with  $\phi$  the mass fraction of the PaRC, as a function of  $|\dot{\gamma}|$  (filled symbols) and  $|\dot{\epsilon}|$  (empty symbols) for three repre-

sentative PaRC with distinct  $L_e$ . For the relatively rigid fd ( $L_e \sim 1$ ), the onset of birefringence occurs at lower values of  $|\dot{\epsilon}|$  than  $|\dot{\gamma}|$ , indicating that fd alignment is induced more readily by extension than by shear [Fig. 3(a)]. We introduce a nondimensional scaling factor ( $SF$ ) to the extension rate as  $SF|\dot{\epsilon}|$  to match the onset of birefringence in extension with that in shear. Practically,  $SF$  provides an estimate of the ratio between the critical shear rate  $|\dot{\gamma}^*|$  and critical extension rate  $|\dot{\epsilon}^*|$  at the onset of PaRC alignment ( $SF = |\dot{\gamma}^*|/|\dot{\epsilon}^*|$ ). For fd,  $SF = 2.3$  captures the difference between extension- and shear-induced alignment at low deformation rates [Fig. 3(b)]. The scaling procedure highlights the difference at high deformation rates where the birefringence in extension reaches a greater plateau value than observed in shear. Using the known dimensions of the fd virus, we compare our experimental results with the revised Doi-Edwards theory for ideal, rigid, and monodisperse rods proposed by Lang *et al.* [11,28]. The theoretical projected order parameter ( $\langle P_2 \rangle$ ) is compared with the experimentally measured birefringence as  $\langle P_2 \rangle \Delta n_0 = \langle \Delta n \rangle / \phi$ , where  $\Delta n_0$  is the birefringence of perfectly aligned PaRC at  $\phi = 1$  [36–38]. To provide a close comparison between theory and the experimental data, in Figs. 3(a) and 3(b) the theoretical curves are scaled as  $\langle P_2 \rangle \Delta n_0$  using  $\Delta n_0 = 0.015$ , a value comparable to a previously reported value for fd [36]. The theory predicts well the birefringence increase with a slope of 1 in both shear and in extension and also

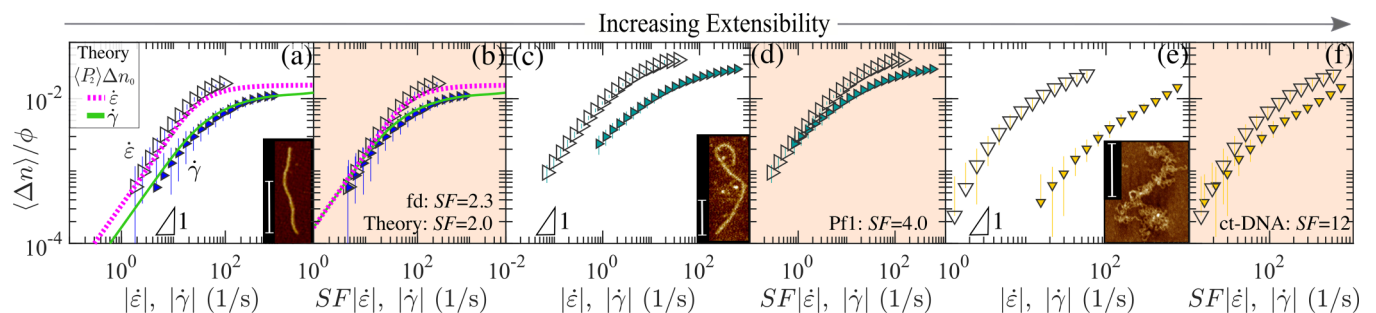


FIG. 3. Spatially averaged birefringence  $\langle \Delta n \rangle$  normalized by the mass fraction of the PaRC  $\phi$  as a function of the extension rate  $|\dot{\epsilon}|$  (empty symbols) and shear rate  $|\dot{\gamma}|$  (filled symbols). (a), (b) fd dispersion at 0.2 mg/mL,  $L_e \sim 1$ . (c), (d) Pf1 dispersion at 0.5 mg/mL,  $L_e \sim 2$ . (e), (f) ct-DNA solution at 0.19 mg/mL,  $L_e \sim 9$ . In (b), (d), and (f) the  $\langle \Delta n \rangle / \phi$  as a function of  $|\dot{\epsilon}|$  is rescaled as  $SF|\dot{\epsilon}|$ . In (a) we provide direct comparison with the order parameter  $\langle P_2 \rangle$  vs  $|\dot{\gamma}|$  and  $|\dot{\epsilon}|$  from the rigid rod theory [11], where  $\langle P_2 \rangle$  is scaled as  $\langle P_2 \rangle \Delta n_0$ . The insets in (a), (c), and (e) are representative AFM images of fd, Pf1, and ct-DNA with a scale bar of 500 nm.

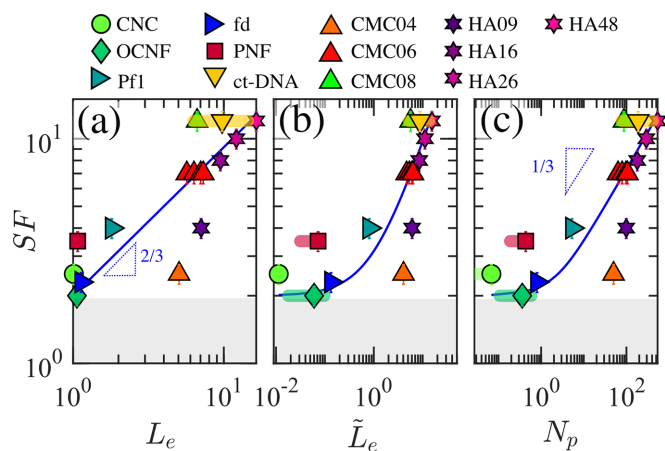


FIG. 4.  $SF$  as a function of  $L_e$ ,  $\tilde{L}_e$ , and  $N_p$ , in (a), (b), and (c), respectively. The solid line in (a) describes  $SF = 2L_e^\beta$ . In (b) the solid line is the plot of  $SF = 2(\tilde{L}_e + 1)^\beta$ , and (c) is the plot of  $SF = 2\left(\sqrt{\frac{N_p^2}{2(N_p + \exp(-N_p) - 1)}}\right)^\beta$ . The gray area sets the threshold  $SF = 2$  for  $L_e = 1$  based on rigid rod theory. For CNC, OCNF, PNF, and ct-DNA the shadowed segments represent the boundaries of  $L_e$ ,  $\tilde{L}_e$ , and  $N_p$  based on the measured contour length distribution [28].

predicts the saturation of birefringence at high deformation rates [Fig. 3(b)]. The theory confirms that (1) a lower extension rate is required to induce fd alignment compared to the shear rate, and that (2) at high deformation rates the greatest extent of alignment occurs in extensional flow. Both (1) and (2) are consistent with the absence of tumbling events in extension, enhancing the overall extent of alignment. For the theoretical curves,  $SF = 2$  (i.e., comparing equal flow strength) enables superimposition of the birefringence curves at low deformation rates in a similar fashion as for the fd dispersion [Fig. 3(b)]. Thus, on the basis of theory  $SF = 2$  is expected in the limiting case of rigid rod-like nanostructures ( $L_e = 1$ ). The slight difference between  $SF$  from the experiment (e.g.,  $SF = 2.3$  for fd) and theory is potentially associated with the fact that fd is not perfectly rigid as assumed by the theory [see inset AFM image in Fig. 3(a)].

With increasing extensibility, the difference between  $|\dot{\epsilon}^*|$  and  $|\dot{\gamma}^*|$  becomes more pronounced, as shown for Pfl [ $L_e \sim 2$ , Figs. 3(c) and 3(d)] and ct-DNA [ $L_e \sim 9$ , Figs. 3(e) and 3(f)]. In these cases, scaling factors of  $SF = 4$  and  $SF = 12$  are required, respectively, to match the onset of birefringence. These results suggest that with the increasing PaRC extensibility, extensional deformations become progressively more effective at inducing the onset of PaRC alignment than shear deformations. Since the effectiveness of the extensional deformations relative to shear deformations at inducing PaRC alignment is captured by  $SF$ , we compare the  $SF$  for a library of PaRC with distinct  $L_e$  [Fig. 4(a)]. In order to highlight the differences between the stiffer PaRC, in Fig. 4(b) we plot  $SF$  as a function of the reduced extensibility parameter  $\tilde{L}_e = (\langle l_c \rangle - \sqrt{\langle R^2 \rangle}) / \sqrt{\langle R^2 \rangle} = L_e - 1$ . Additionally, in Fig. 4(c) we present  $SF$  as a function of  $N_p$ . Although the different chemical structures and architectures of the PaRC investigated lead

to scattering of the data, a general trend of  $SF$  as a function of  $L_e$  emerges. To provide an empirical guideline for future reference, we approximate the  $SF$  increase with  $L_e$  as  $SF = 2L_e^\beta$ , where  $\beta = 2/3$  is a dimensionless parameter [blue line, Fig. 4(a)]. This function also captures the main features for the  $SF$  as a function of  $\tilde{L}_e$  and  $N_p$  in Figs. 4(b) and 4(c), respectively. The trend of  $SF$  as a function of  $N_p$  shows a plateau for  $N_p < 1$  and a transition towards  $SF \propto N_p^{1/3}$  at  $N_p \gtrsim 10$  [Fig. 4(c)]. We physically interpret the evolution of  $SF$  as a function of  $L_e$ ,  $\tilde{L}_e$ , and  $N_p$  based on the flow-induced conformational changes occurring to the PaRC under the contrasting flow types. Rigid PaRC ( $L_e \sim 1$  or  $N_p \ll 1$ ) preserve their rod-like conformation independently of the flow strength and type. Thus, the effectiveness of extensional flows at inducing PaRC alignment ( $SF \sim 2$ ) can be exclusively associated with the absence of tumbling events in extensional flows. However, more extensible or flexible PaRC ( $L_e > 1$ ,  $N_p \gtrsim 1$ ) have the ability to adopt different conformations according to the flow strength and type (e.g., dumbbell, hairpin, etc.) [23,39]. In shear flows intricate conformations and dynamics can occur due to the vorticity component, minimizing the overall degree of backbone orientation. This is supported by single-polymer studies in shear flows, reporting chain extension fluctuation for DNA with  $N_p > 1$ , phenomena not observed in extensional flows [23,40]. Additionally, shear flow has been found to stabilize hairpin conformations for actin filaments with  $N_p \sim 1$  whilst extended conformations have been reported in extensional flows [39,41]. As such, for PaRC with  $N_p \gtrsim 1$ , the enhanced efficacy of extensional deformations at inducing fluid anisotropy, captured by  $SF > 2$ , stems from a more extended conformation occurring in extensional flows compared to shear flows. Note that most experiments were performed in the semidilute regime in order to have sufficient birefringence [28]. By testing some PaRC at different concentrations (i.e., CNC, Pfl, and CMC06, see Supplemental Material [28]), it appears that interparticle interactions in the semidilute regime do not affect significantly the  $SF$ . This is also confirmed by theory for stiff PaRC [28].

Given the key role that PaRC play in many biological and industrial processes (e.g., mucus flow, inkjet printing), there is growing research devoted to studying their dynamics in shear and extensional flows (see, e.g., Refs. [10,21,42,43] and references therein). Here, we experimentally investigate the dynamics of multiple PaRC with different chemistry and architectures to provide a comprehensive understanding of their dynamics in distinct flow conditions. Our results show that the disparity between the critical deformation rates required for the onset of PaRC alignment in shear and extension is related to PaRC extensibility. We hope that our framework of analysis and derived scaling concepts will be tested by numerical simulations and prove beneficial for synthesising materials with anisotropic microstructures.

The authors gratefully acknowledge the support of Okinawa Institute of Science and Technology Graduate University with subsidy funding from the Cabinet Office, Government of Japan. V.C. and S.J.H. also acknowledge financial support from the Japan Society for the Promotion of Science (JSPS, Grants No. 22K14738 and No. 21K03884).

- [1] M. Rubinstein and R. H. Colby, *Polymer Physics* (Oxford University Press, New York, 2003).
- [2] M. Doi and S. F. Edwards, *The Theory of Polymer Dynamics* (Oxford University Press, New York, 1988).
- [3] T. Rosén, B. S. Hsiao, and L. D. Söderberg, Elucidating the opportunities and challenges for nanocellulose spinning, *Adv. Mater.* **33**, 2001238 (2021).
- [4] Y.-J. Chen, D. Wu, W. Gelbart, C. M. Knobler, R. Phillips, and W. K. Kegel, Two-stage dynamics of in vivo bacteriophage genome ejection, *Phys. Rev. X* **8**, 021029 (2018).
- [5] P. Grayson, L. Han, T. Winther, and R. Phillips, Real-time observations of single bacteriophage  $\lambda$  DNA ejections in vitro, *Proc. Natl. Acad. Sci. USA* **104**, 14652 (2007).
- [6] E. K. Hill, B. Krebs, D. G. Goodall, G. J. Howlett, and D. E. Dunstan, Shear flow induces amyloid fibril formation, *Biomacromolecules* **7**, 10 (2006).
- [7] C. Akkermans, A. J. van der Goot, P. Venema, E. van der Linden, and R. M. Boom, Formation of fibrillar whey protein aggregates: Influence of heat and shear treatment, and resulting rheology, *Food Hydrocolloids* **22**, 1315 (2008).
- [8] R. H. Colby, Structure and linear viscoelasticity of flexible polymer solutions: Comparison of polyelectrolyte and neutral polymer solutions, *Rheol. Acta* **49**, 425 (2010).
- [9] Note that  $|E| \equiv \dot{\gamma}$  for the shear rate and  $|E| \equiv \dot{\epsilon}$  for the extension rate; the extension rate  $\dot{\epsilon}$  refers to the streamwise velocity gradient and the shear rate  $\dot{\gamma}$  refers to the velocity gradient normal to the flow direction.
- [10] V. Calabrese, A. Q. Shen, and S. J. Haward, Naturally derived colloidal rods in microfluidic flows, *Biomicrofluidics* **17**, 021301 (2023).
- [11] C. Lang, J. Kohlbrecher, L. Porcar, A. Radulescu, K. Sellinghoff, J. K. G. Dhont, and M. P. Lettinga, Microstructural understanding of the length- and stiffness-dependent shear thinning in semidilute colloidal rods, *Macromolecules* **52**, 9604 (2019).
- [12] M. Doi and S. F. Edwards, Dynamics of rod-like macromolecules in concentrated solution. Part 1, *J. Chem. Soc., Faraday Trans. 2* **74**, 560 (1978).
- [13] J. K. G. Dhont and W. J. Briels, *Soft Matter* (Wiley-VCH, Weinheim, 2005), Vol. 2.
- [14] A. Zöttl, K. E. Klop, A. K. Balin, Y. Gao, J. M. Yeomans, and D. G. Aarts, Dynamics of individual Brownian rods in a microchannel flow, *Soft Matter* **15**, 5810 (2019).
- [15] V. Calabrese, S. J. Haward, and A. Q. Shen, Effects of shear- and extensional flows on the alignment of colloidal rods, *Macromolecules* **54**, 4176 (2021).
- [16] V. Calabrese, C. György, S. J. Haward, T. J. Neal, S. P. Armes, and A. Q. Shen, Microstructural dynamics and rheology of worm-like diblock copolymer nanoparticle dispersions under a simple shear and a planar extensional flow, *Macromolecules* **55**, 10031 (2022).
- [17] P. T. Corona, B. Berke, M. Guizar-Sicairos, L. G. Leal, M. Liebi, and M. E. Helgeson, Fingerprinting soft material nanostructure response to complex flow histories, *Phys. Rev. Mater.* **6**, 045603 (2022).
- [18] B. Chun and H. W. Jung, Universal flow-induced orientational ordering of colloidal rods in planar shear and extensional flows: Dilute and semidilute concentrations, *J. Rheol.* **67**, 315 (2023).
- [19] P. G. De Gennes, Coil-stretch transition of dilute flexible polymers under ultrahigh velocity gradients, *J. Chem. Phys.* **60**, 5030 (1974).
- [20] A. Keller and J. A. Odell, The extensibility of macromolecules in solution; A new focus for macromolecular science, *Colloid Polym. Sci.* **263**, 181 (1985).
- [21] C. M. Schroeder, Single polymer dynamics for molecular rheology, *J. Rheol.* **62**, 371 (2018).
- [22] R. Larson and J. Magda, Coil-stretch transitions in mixed shear and extensional flows of dilute polymer solutions, *Macromolecules* **22**, 3004 (1989).
- [23] D. E. Smith, H. P. Babcock, and S. Chu, Single-polymer dynamics in steady shear flow, *Science* **283**, 1724 (1999).
- [24] J. S. Hur, E. S. G. Shaqfeh, H. P. Babcock, and S. Chu, Dynamics and configurational fluctuations of single DNA molecules in linear mixed flows, *Phys. Rev. E* **66**, 011915 (2002).
- [25] S. J. Haward, M. S. N. Oliveira, M. A. Alves, and G. H. McKinley, Optimized cross-slot flow geometry for microfluidic extensional rheometry, *Phys. Rev. Lett.* **109**, 128301 (2012).
- [26] S. J. Haward, G. H. McKinley, and A. Q. Shen, Elastic instabilities in planar elongational flow of monodisperse polymer solutions, *Sci. Rep.* **6**, 33029 (2016).
- [27] G. G. Fuller, *Optical Rheometry of Complex Fluids* (Oxford University Press, New York, 1995).
- [28] See Supplemental Material at <http://link.aps.org/supplemental/10.1103/PhysRevResearch.6.L012042> for the detailed information of the PaRC and their rheological characterization, including Refs. [15,21,26,30–35,44,45,45–53].
- [29] N. Burshtein, S. T. Chan, K. Toda-Peters, A. Q. Shen, and S. J. Haward, 3D-printed glass microfluidics for fluid dynamics and rheology, *Curr. Opin. Colloid Interface Sci.* **43**, 1 (2019).
- [30] S. J. Haward, Characterization of hyaluronic acid and synovial fluid in stagnation point elongational flow, *Biopolymers* **101**, 287 (2014).
- [31] I. Usov and R. Mezzenga, FiberApp: An open-source software for tracking and analyzing polymers, filaments, biomacromolecules, and fibrous objects, *Macromolecules* **48**, 1269 (2015).
- [32] C. G. Lopez, R. H. Colby, and J. T. Cabral, Electrostatic and hydrophobic interactions in NaCMC aqueous solutions: Effect of degree of substitution, *Macromolecules* **51**, 3165 (2018).
- [33] T. Norisuye, Conformation and solution properties of water-soluble polysaccharides: Case study of hyaluronic acid, in *Hydrocolloids* (Elsevier, New York, 2000), pp. 311–320.
- [34] K. Salamon, D. Aumiler, G. Pabst, and T. Vuletich, Probing the mesh formed by the semirigid polyelectrolytes, *Macromolecules* **46**, 1107 (2013).
- [35] W. Reisner, J. N. Pedersen, and R. H. Austin, DNA confinement in nanochannels: Physics and biological applications, *Rep. Prog. Phys.* **75**, 106601 (2012).
- [36] K. R. Purdy, Z. Dogic, S. Fraden, A. Rühm, L. Lurio, and S. G. J. Mochrie, Measuring the nematic order of suspensions of colloidal fd virus by x-ray diffraction and optical birefringence, *Phys. Rev. E* **67**, 031708 (2003).
- [37] K. Uetani, H. Koga, and M. Nogi, Estimation of the intrinsic birefringence of cellulose using bacterial cellulose nanofiber films, *ACS Macro Lett.* **8**, 250 (2019).
- [38] T. Rosén, R. Wang, C. Zhan, H. He, S. Chodankar, and B. S. Hsiao, Cellulose nanofibrils and nanocrystals in

- confined flow: Single-particle dynamics to collective alignment revealed through scanning small-angle x-ray scattering and numerical simulations, *Phys. Rev. E* **101**, 032610 (2020).
- [39] I. Kirichenbuechler, D. Guu, N. A. Kurniawan, G. H. Koenderink, and M. P. Lettinga, Direct visualization of flow-induced conformational transitions of single actin filaments in entangled solutions, *Nat. Commun.* **5**, 5060 (2014).
- [40] C. M. Schroeder, R. E. Teixeira, E. S. G. Shaqfeh, and S. Chu, Characteristic periodic motion of polymers in shear flow, *Phys. Rev. Lett.* **95**, 018301 (2005).
- [41] Y. Liu, K. Zografos, J. Fidalgo, C. Duchêne, C. Quintard, T. Darnige, V. Filipe, S. Huille, O. Du Roure, M. S. Oliveira, and A. Lindner, Optimised hyperbolic microchannels for the mechanical characterisation of bio-particles, *Soft Matter* **16**, 9844 (2020).
- [42] J. Dinic, C. D. V. Martínez Narváez, and V. Sharma, Rheology of unentangled polymer solutions depends on three macromolecular properties: Flexibility, extensibility, and segmental dissymmetry, in *Macromolecular Engineering*, edited by N. Hadjichristidis, Y. Gnanou, K. Matyjaszewski, and M. Muthukumar (Wiley, Hoboken, NJ, 2022).
- [43] A. Lindner, Morphological transitions of flexible fibers in viscous flows, *Science Talks* **3**, 100057 (2022).
- [44] C. G. Lopez and W. Richtering, Conformation and dynamics of flexible polyelectrolytes in semidilute salt-free solutions, *J. Chem. Phys.* **148**, 244902 (2018).
- [45] J. Sambrook, E. Fritsch, and T. Maniatis, *Molecular Cloning: A Laboratory Manual* (Cold Spring Harbour Laboratory Press, New York, 1989).
- [46] V. Calabrese, S. Varchanis, S. J. Haward, and A. Q. Shen, Alignment of colloidal rods in crowded environments, *Macromolecules* **55**, 5610 (2022).
- [47] P. Bertsch, A. Sánchez-Ferrer, M. Bagnani, S. Isabetini, J. Kohlbrecher, R. Mezzenga, and P. Fischer, Ion-induced formation of nanocrystalline cellulose colloidal glasses containing nematic domains, *Langmuir* **35**, 4117 (2019).
- [48] R. Tanaka, T. Saito, D. Ishii, and A. Isogai, Determination of nanocellulose fibril length by shear viscosity measurement, *Cellulose* **21**, 1581 (2014).
- [49] T. P. Santos, V. Calabrese, M. W. Boehm, S. K. Baier, and A. Q. Shen, Flow-induced alignment of protein nanofibril dispersions, *J. Colloid Interface Sci.* **638**, 487 (2023).
- [50] B. Barabé, S. Abakumov, D. Z. Gunes, and M. P. Lettinga, Sedimentation of large particles in a suspension of colloidal rods, *Phys. Fluids* **32**, 053105 (2020).
- [51] L. M. Bravo-Anaya, M. Rinaudo, and F. A. Soltero Martínez, Conformation and rheological properties of calf-thymus DNA in solution, *Polymers* **8**, 51 (2016).
- [52] C. G. Lopez, R. H. Colby, P. Graham, and J. T. Cabral, Viscosity and scaling of semiflexible polyelectrolyte NaCMC in aqueous salt solutions, *Macromolecules* **50**, 332 (2017).
- [53] C. G. Lopez and W. Richtering, Influence of divalent counterions on the solution rheology and supramolecular aggregation of carboxymethyl cellulose, *Cellulose* **26**, 1517 (2019).